ACS APPLIED MATERIALS & INTERFACES

Research Article

Cite This: ACS Appl. Mater. Interfaces 2019, 11, 17467−17474

www.acsami.org

Three-Dimensional Branched Crystal Carbon Nitride with Enhanced Intrinsic Peroxidase-Like Activity: A Hypersensitive Platform for Colorimetric Detection

Yaofang Fan, Weican Zhang, Yanming Liu, Zhenxing Zeng, Xie Quan, and Huimin Zhao*

Key Laboratory of Industrial Ecology and Environmental Engineering (Ministry of Education, China), School of Environmental Science and Technology, Dalian University of Technology, Dalian 116024, China

Supporting Information

ABSTRACT: Graphitic carbon nitride (g-C_3N_4) as a metal-free nanozyme has attracted huge attention for catalytic applications. However, the catalytic activity of pure g-C_3N_4 causes very moderate H_2O_2 activation. Herein, a novel three-dimensional (3D) branched carbon nitride nanoneedle (3DBC-C_3N_4) nanozyme has been proposed to overcome such shortcoming. This unique 3D branched structure of 3DBC-C_3N_4 facilitated effective mass transfer during catalytic reaction and induced a lightning rodlike effect to accelerate electron collection at the tip area for H_2O_2 activation. With improved H_2O_2 activation for hydroxyl radical ($^{\bullet}OH$) generation, 3DBC-C_3N_4 showed excellent peroxidase-like activity toward 3,3′,5,5′-tetramethylbenzidine oxidation in the presence of H_2O_2. As for H_2O_2, the V_{max} value of 3DBC-C_3N_4 was found to be 20 times higher than that of natural horseradish peroxidase. Moreover, the 3D branched structure of 3DBC-C_3N_4 offered large interface for the reversible conjugation of single-stranded DNA, which enhanced the colorimetric sensitivity. Moreover, 3DBC-C_3N_4 exhibited high sensitivity toward oxytetracycline detection, with the detection limit and quantitative limit of 1 and 50 μg/L, respectively.

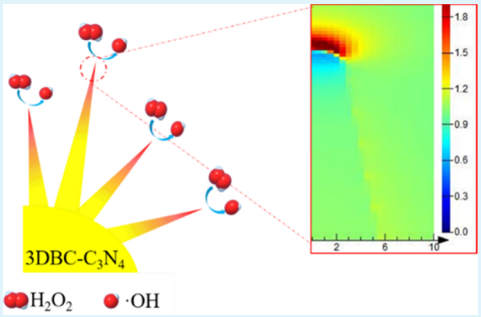

KEYWORDS: *g-C_3N_4, nanoneedles, peroxidase-like, DNA, biosensor*

INTRODUCTION

Natural enzymes are made up of protein molecules that are considered to be highly selective toward their substrates. This highly selective nature of enzymes makes them suitable for multiple scientific applications.[1] However, inherent instability toward external environment, limited resources, and high cost of processing limit the extended applications of enzymes in various fields. To overcome this, nanozymes nanomaterials are considered as interesting alternatives that possess natural-enzyme-like activity. In recent times, nanozymes have withdrawn considerable attention as biosensors due to their low fabrication cost, high resistance to biodegradation, and bulk preparation schemes.[2,3] For instance, Fe_3O_4 nanoparticles were discovered as nanozymes, which possessed intrinsic peroxidase-like activity to oxidize substrates in the presence of H_2O_2 to form colored reaction products.[4] Furthermore, a number of nanozymes such as quantum dots,[5−7] noble metals,[8] metal oxide nanoparticles,[9,10] and carbon nanomaterials[11,12] have been extensively employed for the development of colorimetric biosensors that possess peroxidase-like activity. However, the catalytic efficiency of most of the artificial enzymes is still unsatisfied when compared to that of natural enzymes. Although the core of nanozyme is active, the catalytic reactions merely take place at the surface of nanozymes. Thus, the catalytic performance of nanozymes is strictly affected by the density and reactivity of the active sites at the surface and also by their poor electronic transport properties.[13] Therefore, engineering the surface to proliferate the number of active sites is highly essential to enhance the number of active sites and thus their catalytic efficiency.

Graphitic carbon nitride (g-C_3N_4) is considered as one of most abundant carbon nanomaterials that has been potentially explored in the field of photocatalysis,[14−17] electrochemical catalysis,[18−21] and biosensors[22−25] due to its good water hydrophilic performance and high thermal and chemical stability.[26] Reportedly, Sun et al. found that g-C_3N_4 possessed intrinsic peroxidase-like activity.[27] Consequently, g-C_3N_4 has been employed as colorimetric biosensor for H_2O_2 and glucose[28,29] in the past few years. Similar to other carbon nanomaterials,[30−34] g-C_3N_4 has demonstrated to absorb single-stranded DNA (ssDNA) rather than double-stranded DNA. The high affinity between g-C_3N_4 and ssDNA has enabled specific recognition of targets molecules using g-C_3N_4/DNA-sensing platforms.[35] However, most of the reported g-C_3N_4-based nanozymes are in the form of nanosheets, which undergo aggregation and pore deformation, leading to the loss of active sites during sensing applications.[36] Further, presence of defects at the surface of g-C_3N_4 nanozymes blocks the

Received: March 10, 2019
Accepted: April 25, 2019
Published: April 25, 2019

DOI: 10.1021/acsami.9b04320
ACS Appl. Mater. Interfaces 2019, 11, 17467−17474

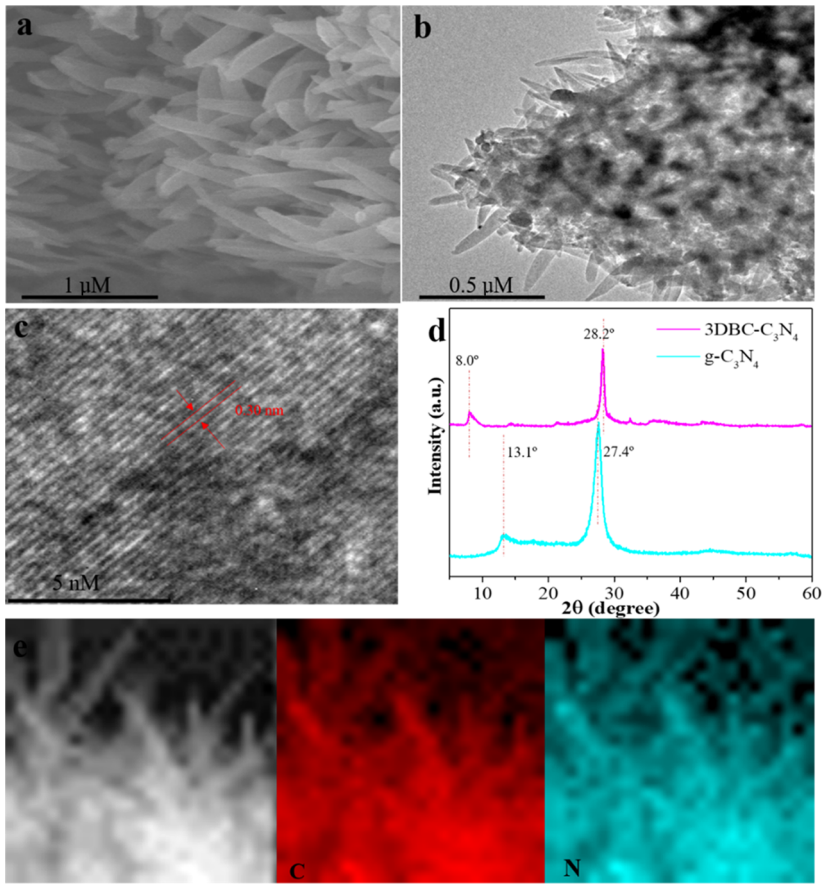

Figure 1. SEM (a), TEM (b), and HRTEM (c) images of 3DBC-C_3N_4. XRD pattern (d) of 3DBC-C_3N_4 and g-C_3N_4. EDX mapping images (e) of elemental C and N in the selected area.

electron-transport properties along the in-plane directions.[37] Moreover, structural agglomerates retard the mass transfer efficiency of g-C_3N_4 nanozymes during catalytic reactions. Therefore, breakthrough in structure adjustment is of utmost significance to overcome the above said shortcomings.

In this regard, preparation of three-dimensional (3D) branched morphology of nanomaterials has been proved to be highly promising for various catalytic applications. Such 3D branched nanostructures have been successfully applied in Raman scattering,[38] H_2O_2 decomposition,[39] and CO_2 reduction[40] reactions. For example, Kelley et al. prepared sharp-tip nanoneedle structures possessing high local electric field for efficient CO_2 reduction.[40] The 3D branched nanostructures possess highly effective surface area, which facilitates large number of active sites to absorb more target molecules for catalytic reactions. Thus, fabricating 3D branched g-C_3N_4 with a sharp-tip nanostructure can be considered as an effective strategy for improving its enzyme-like performance.

The present paper reports the design and preparation of a novel 3D g-C_3N_4 with appreciably increased density of one-dimensional (1D) crystal nitride nanoneedles (3DBC-C_3N_4) as an artificial enzyme. Based on Lineweaver–Burk equation, the intrinsic catalytic activity performance of 3DBC-C_3N_4 was employed in the presence of H_2O_2-containing peroxidase substrate 3,3′,5,5′-tetramethylbenzidine (TMB). The mechanism for high peroxidase-like activity performance of 3DBC-C_3N_4 was discussed together with 3D finite-difference time-domain (FDTD) calculation. Furthermore, the conjugation effect of ssDNA on peroxidase-like activity performance of 3DBC-C_3N_4 was investigated for developing a sensitive and selective colorimetric method for oxytetracycline (OTC) detection.

RESULTS AND DISCUSSION

Structural Characterization. In this present work, the 3D branched crystalline carbon nitride with nanoneedles was fabricated via a modified ionothermal synthetic process.[41] The structural morphology of the prepared 3DBC-C_3N_4 was characterized by scanning electron microscopy (SEM). Figures 1a and S1 clearly present the typical 3D branched crystal structures of 3DBC-C_3N_4 composed of 1D nanoneedles. The 3D branched morphology is also an important factor to inhibit material aggregation,[42,43] which further could induce weak van der Waals force interactions between the interface to prevent aggregation compared to g-C_3N_4 (Figure S2). Based on the acquired transmission electron microscopy (TEM) images (Figure 1b), nanoneedles of 3DBC-C_3N_4 were found to be packed uniformly and tightly. The morphologies of the nanoneedles were radially formed from large diameters to small diameters and finally terminated at high-curvature tips. Further, high-magnification TEM (HRTEM) image shows the lattice fringes of 3DBC-C_3N_4 with an interplane distance of 0.3 nm (Figure 1c). This corresponded to the (002) plane of carbon nitride and was found to be consistent with the previous reports[44] demonstrating similar crystalline nature of 3DBC-C_3N_4 as that of bulk g-C_3N_4. The crystal structure of 3DBC-C_3N_4 was further confirmed by X-ray diffraction (XRD) studies. As demonstrated in Figure 1d, pure g-C_3N_4 and

DOI: 10.1021/acsami.9b04320
ACS Appl. Mater. Interfaces 2019, 11, 17467−17474

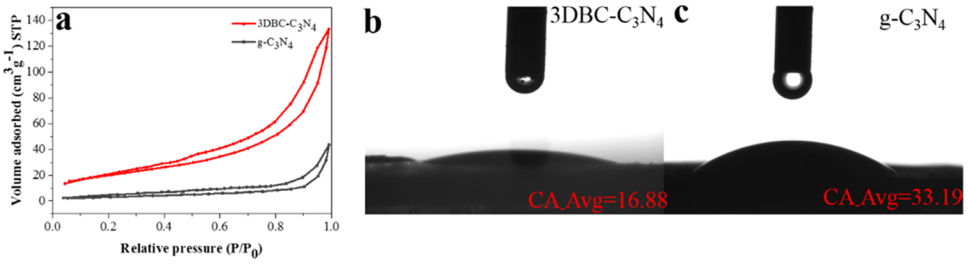

Figure 2. Nitrogen gas adsorption/desorption isotherms (a) and water contact angle of 3DBC-C_3N_4 (b) and g-C_3N_4 (c).

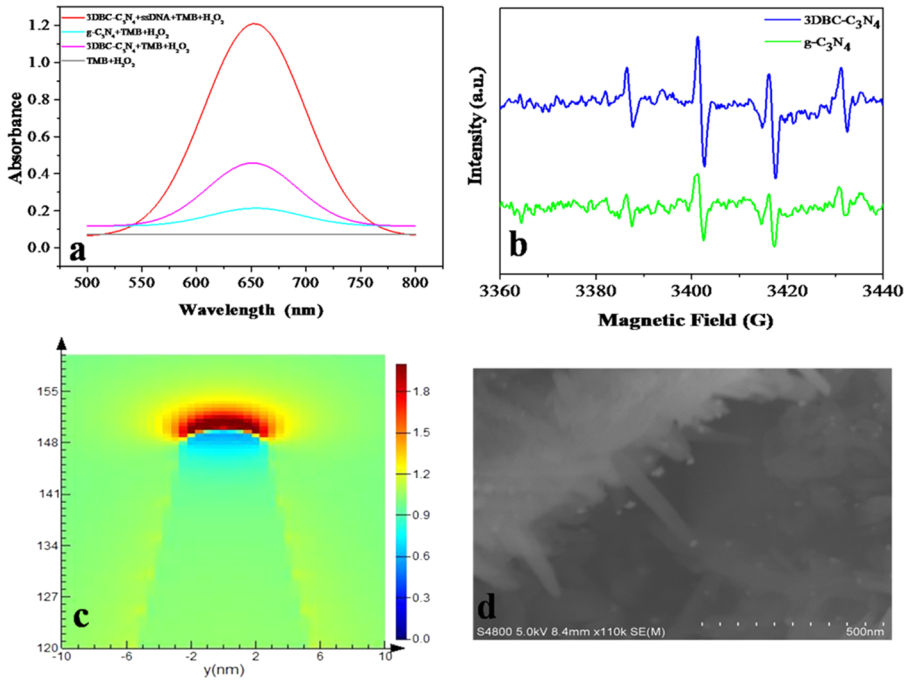

Figure 3. UV−vis absorption spectra of different reaction systems (a). EPR spectra of 3DBC-C_3N_4 and g-C_3N_4 with 5,5-dimethyl-1-pyrroline-*N*-oxide-OH (b). Electric field distribution of 3BDC-C_3N_4 nanoneedles (c). SEM image of 3BDC-C_3N_4 nanoneedles with deposited Au particles (d).

3DBC-C_3N_4 both show two characterized peaks but are located in different places. For g-C_3N_4, the characteristic peaks at 2θ of 13.1 and 27.4° were attributed to the in-plane repeating motif of (100) plane and the intralayer stacking motif indexed (002) plane, respectively.[41,45,46] Compared to g-C_3N_4, the (100) plane of 3DBC-C_3N_4 shifted from 13.1 to 8.0° due to the more stretched in-plane structure. The more stretched in-plane structure resulted in improved in-plane periodic nature and therefore an improved intralayer stacking shown by the (002) plane, which shifted from 27.4 to 28.2°. The energy-dispersive X-ray spectroscopy (EDX) elemental mappings (Figure 1e) of C and N elements reveal that carbon and nitrogen have similar shape and location dispersed in the sample, indicating that C and N elements are well dispersed over the nanomaterials.

Both surface area and porosity of 3DBC-C_3N_4 and g-C_3N_4 were investigated by nitrogen adsorption−desorption isotherms, as shown in Figures 2a and S3, respectively. 3DBC-C_3N_4 and g-C_3N_4 both gave rise to H1-type nitrogen gas sorption. The surface area of 3DBC-C_3N_4 was 73.183 m^2/g, which was 5 times higher than that of g-C_3N_4 with surface area of 14.529 m^2/g. The enhanced surface area was ascribed to abundant mesopores and 3D nanostructural morphology of 3DBC-C_3N_4. The results suggested the high efficiency of 3DBC-C_3N_4 to provide large number of active sites for substrate absorption. Furthermore, the hydrophilic nature of the nonstructural surface helped in interacting with the surrounding water environment. To specify the wettability of 3DBC-C_3N_4, the water contact angles of 3DBC-C_3N_4 (16.88°) and g-C_3N_4 (33.19°) were also measured as shown in Figure 2b,c, respectively. A hydrophilic surface with a lower water contact angle of 3DBC-C_3N_4 was obtained owing to strong O−H stretches of 3DBC-C_3N_4 at 3000−3500 cm^{-1} (Figure S4). The results suggested that the prepared 3DBC-C_3N_4 possessed a water-favorable wetting performance, offering a good opportunity to be applied as nanozyme in aqueous environment.

Peroxidase-Like Enzyme Mimetic Properties and Possible Catalytic Mechanism of 3DBC-C_3N_4. To evaluate the peroxidase-like activity of the prepared 3DBC-C_3N_4, the catalytic oxidation of TMB substrate was tested in the presence of H_2O_2. Under similar optimal experimental condition, the synergistic catalytic property of 3DBC-C_3N_4 and g-C_3N_4 has been presented in Figure 3a, which shows an enhanced peroxidase-like activity of 3DBC-C_3N_4 compared to that of g-C_3N_4. To understand the mechanism of catalytic activity of 3DBC-C_3N_4, steady-state kinetic parameters were determined for a comparative analysis of peroxidase-like catalytic activities of 3DBC-C_3N_4, g-C_3N_4, and HRP toward TMB and H_2O_2. Michaelis−Menten constant (K_m) and maximal velocity (V_{max})

DOI: 10.1021/acsami.9b04320
ACS Appl. Mater. Interfaces 2019, 11, 17467−17474

Table 1. Comparison of K_m and V_{max} of 3DBC-C_3N_4 with ssDNA, 3DBC-C_3N_4, g-C_3N_4, and HRP

peroxidase mimics	substrate	K_m (mM)	V_{max} (10^{-7} M s^{-1})	reference
3DBC-C_3N_4 with ssDNA	TMB	0.0286	25.2	this work
	H_2O_2	0.0712	33.5	
3DBC-C_3N_4	TMB	0.0442	20.5	this work
	H_2O_2	0.0781	31.8	
g-C_3N_4	TMB	0.0768	19.3	this work
	H_2O_2	0.184	19.3	
HRP	TMB	0.210	0.800	47
	H_2O_2	4.57	1.40	

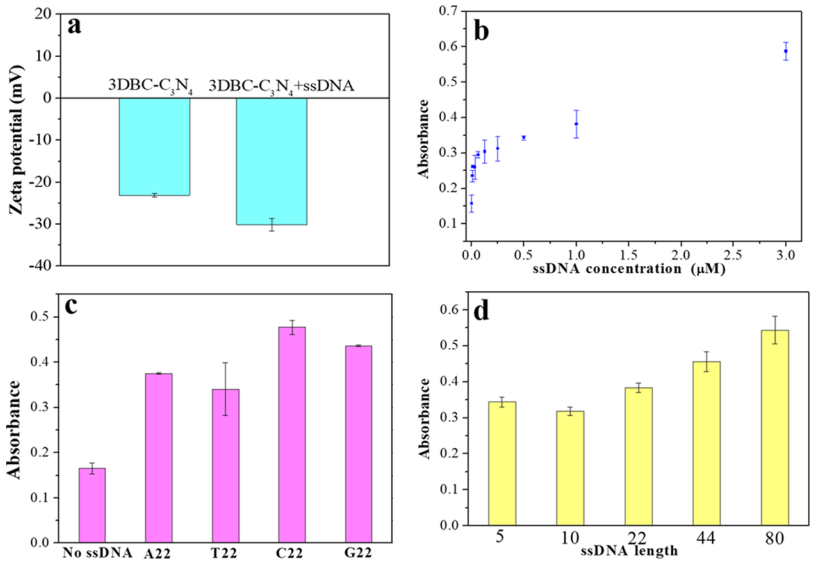

Figure 4. ζ-Potential of 3DBC-C_3N_4 with or without ssDNA at pH 4 (a). The effect of ssDNA concentration (b), ssDNA composition (c), and ssDNA length (d) on the peroxidase-like activity of 3DBC-C_3N_4.

of 3DBC-C_3N_4, g-C_3N_4, and horse reddish peroxidase (HRP) was calculated by Lineweaver−Burk equation (Table 1). Compared to that of g-C_3N_4, the K_m value of 3DBC-C_3N_4 was found to be lower, indicating a stronger affinity of 3DBC-C_3N_4 toward TMB. This further helped in achieving a higher V_{max} toward TMB. Notably, the K_m value of 3DBC-C_3N_4 toward H_2O_2 was much lower than that of g-C_3N_4, demonstrating the higher affinity of 3DBC-C_3N_4 toward H_2O_2 substrate compared to that of g-C_3N_4. Further, as for H_2O_2, the apparent V_{max} value of 3DBC-C_3N_4 was found to be higher than that of g-C_3N_4. In addition, the V_{max} value of 3DBC-C_3N_4 for H_2O_2 and TMB was observed to be 20 times higher than that of HRP. Electron paramagnetic resonance (EPR) was further investigated for confirming the mechanism of catalytic activity of 3DBC-C_3N_4. As shown in Figure 3b, the signal intensity of $^{\bullet}OH$ generated by the deposition of H_2O_2 was dramatically high with the addition of 3DBC-C_3N_4 compared to g-C_3N_4. This demonstrated that the massive $^{\bullet}OH$ production was induced by the activation of H_2O_2 in the presence of 3DBC-C_3N_4.

Apart from the combined advantages of high crystallinity, large surface area, and hydrophilic interaction, the directional confinement inevitable for charge separation and rapid electronic transmission are other key factors for H_2O_2 activation. Nanoneedles with high local electric field at the sharp tips can concentrate substrate molecules near the active catalytic surface for catalysis applications.[40] To investigate the effect of sharpness on H_2O_2 catalysis, FDTD calculation was carried out to stimulate the prospects of tip-enhanced nanometer-scale electric field intensification. Figure 3c shows the unsymmetric electric field distribution on the nanorods. Electric field intensity increased gradually from large diameters to intermediate diameters and finally to the high-curvature nanoneedles. The highest curvature area of the tip of 3DBC-C3N4 possesses the maximum electric field intensity, which is originated from the locally concentrated free-electron leaded via the electrostatic repulsion. The local concentrated electric field at the tips of 3DBC-C_3N_4 accelerates the H_2O_2 deposition for further catalysis due to accelerating charge collection and separation. The enhanced charge collection at the tip area of 3DBC-C_3N_4 was further verified via in situ photodeposition of Au nanoparticles. After the deposition, the SEM image of Figure 3d clearly exhibits that most of the Au nanoparticles are located on the tips of the 3DBC-C_3N_4 nanoneedles. It is favorable for the free electrostatic migrates of 3DBC-C3N4 at sharpest curvature regions as a consequence in accordance with FDTD calculated results in above. The result further indicated that a lower tip radius at the 3DBC-C_3N_4 needle tips generated a higher electric field concentration that accumulated H_2O_2 concentration to enhance the production of $^{\bullet}OH$. Remarkably, the prepared 3DBC-C_3N_4 exhibited greatly improved catalytic performance, which could be ascribed to its high crystallinity, large surface area, and high hydrophilcity. More importantly, the catalytic reaction was highly associated with charge separation and high electron concentration of nanoneedles for H_2O_2 activation.

DOI: 10.1021/acsami.9b04320
ACS Appl. Mater. Interfaces 2019, 11, 17467−17474

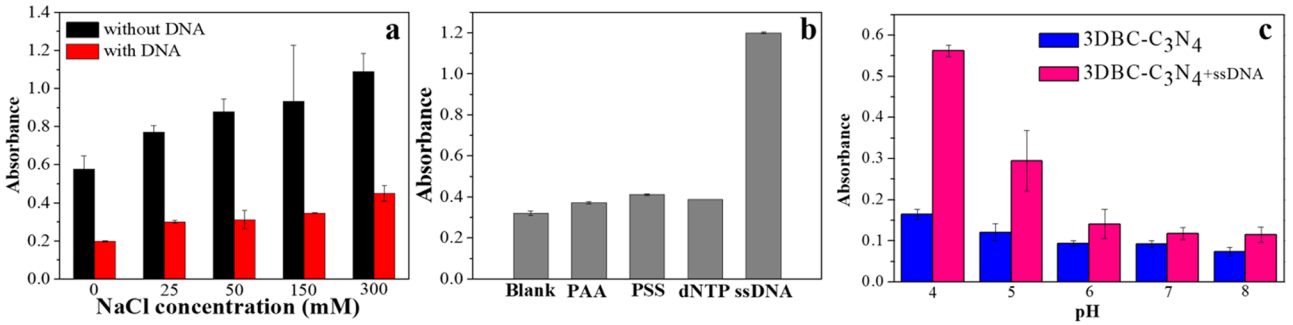

Figure 5. Oxidation of ABTS (a) at various NaCl concentration for 3DBC-C_3N_4 with or without ssDNA. TMB oxidation enhancement of 3DBC-C_3N_4 coated with various negatively charged polymer (b). pH values of 3DBC-C_3N_4 with or without ssDNA on the TMB oxidation catalysis (c).

ssDNA-Regulated Peroxidase-Like Activity of 3DBC-C_3N_4 Assays. Previous reports have shown that the peroxidase activity of various traditional nanomaterials such as graphene and carbon nanotubes can be regulated by ssDNA owing to the interaction between ssDNA and nanomaterials. This property has successfully led to the development of various colorimetric biosensor platform in the past few years.[12,48] Next, ssDNA, taking aptamer of OTC as an example,[49] regulating the peroxidase catalytic activity of 3DBC-C_3N_4 was investigated to explore potential application. After adding ssDNA aptamer of OTC, peroxidase catalytic activity of 3DBC-C_3N_4 was investigated in Figure 3a. The peroxidase-like activity of 3DBC-C_3N_4 was found to be dependent on the incubation time (a), pH (b), TMB concentration, (c) and temperature (d) as shown in Figure S5. A concentration of 5 mM for TMB and 50 mM for H_2O_2, 30 min as incubation time, 25−28 °C as room temperature, and pH 4 were chosen optimum experimental conditions. Interestingly, after adding ssDNA, the higher UV−vis absorbance was observed compared to bare 3DBC-C_3N_4 (Figure 3a), which indicated that ssDNA upregulated the peroxidase catalytic activity of 3DBC-C_3N_4. To evaluate the multiplexing effect of ssDNA on the peroxidase-like catalytic activities of 3DBC-C_3N_4, the values of K_m and V_{max} toward H_2O_2 or TMB were first determined by Lineweaver−Burk equation, which has been summarized in Table 1. Te K_m value of 3DBC-C_3N_4 with ssDNA toward TMB was found to be much lower than that of 3DBC-C_3N_4, which clearly indicated that ssDNA increased the affinity to 3DBC-C_3N_4. Recent reports demonstrate that DNA can accelerate Fe_3O_4 for TMB absorption via electrostatic interaction at pH 4.[50] The ζ-potential was measured for exploring the importance of electrostatic interaction between 3DBC-C_3N_4, ssDNA, and TMB. After adsorbing ssDNA, ζ-potential value was observed to be more negatively charged (−30.15) than that of 3DBC-C_3N_4 (−23.15) at pH 4 (Figure 4a). The nonoxidized TMB (pK_a 4.2) was found to be partially positively charged in the operation condition (pH = 4), which contributed to the affinity to ssDNA-functionalized 3DBC-C_3N_4 for further oxidation due to electrostatic incorporation. As a result, the V_{max} value of 3DBC-C_3N_4 with ssDNA toward TMB was found to be much higher than that of 3DBC-C_3N_4. The K_m value and V_{max} value of 3DBC-C_3N_4 with ssDNA showed no obvious differences when compared to those of 3DBC-C_3N_4 without ssDNA. This revealed that the enhanced peroxidase-like activity of 3DBC-C_3N_4 with ssDNA was not derived from accelerating H_2O_2 decomposition.

To further evaluate the effect of ssDNA on TMB oxidation, ssDNA concentration, ssDNA composition, and ssDNA length on 3DBC-C_3N_4 toward TMB oxidation were tested. The TMB oxidation using 3DBC-C_3N_4 with ssDNA gradually enhanced with increasing concentration of ssDNA from 0 to 3 μM (Figure 4b), which further illustrated the effect of ssDNA for TMB adsorption for oxidation via aromatic stacking such as hydrogen bonding and $\pi-\pi$ stacking. The order of peroxidase-like activity of 3DBC-C_3N_4 with 22-mer homo DNAs (A22, T22, C22, and G22) sequence was poly C > poly G > poly A > poly T > no ssDNA (Figure 4c), which was ascribed to the secondary structure and electrostatic incorporation of ssDNA producing different interactions. Parts of ssDNA was protonated at pH 4, especially for cytosine, due to pK_a values of adenine (4.2), thymine (9.9), cytosine (3.5), and guanine (2.1 and 9.2). Therefore, a large fraction of protonated ssDNA neutralized some charge on the surface of 3DBC-C_3N_4 and weakened the repulsion among ssDNA. This resulted in more ssDNA adsorption to 3DBC-C_3N_4 surface and accelerated TMB oxidation. Varied length of poly C was used to estimate the ssDNA length impact on the peroxidase-like activity of 3DBC-C_3N_4 under the same total nucleotide concentrations (e.g., the concentration of the C80 is 16 times lower than that of C5). On the whole, the activity of TMB oxidation is positively related to the length of ssDNA (Figure 4d). Even though the molar concentration of C80 was the lowest, 3DBC-C_3N_4 with C80 exhibited the most enhanced peroxidase-like activity. Longer ssDNA likely provided higher affinity to 3DBC-C_3N_4 due to large number of exposed binding sites, such as polyvalent binding effect.[51] This further indicated that the peroxidase-like activity was likely derived from the interfacial effect after 3DBC-C_3N_4 was bound to ssDNA.

Aforementioned finding reveals that ssDNA-functionalized 3DBC-C_3N_4 facilitates the TMB affinity for oxidation via electrostatic incorporation. To evaluate the conjecture, 2,2′-azino-bis(3-ethylbenzthiazoline-6-sulfonic acid) (ABTS) was employed as a negatively charged substrate that possessed dual sulfate anions. In the presence of ssDNA, the oxidation of ABTS was inhibited due to charge repulsion between the surface of 3DBC-C_3N_4 with ssDNA and ABTS (Figure 5a). To further verify the mechanism of electrostatic incorporation, the oxidation of ABTS was tested in different NaCl concentrations. After increasing the NaCl concentration, the oxidation performance of ABTS recovered gradually by screening charge repulsion between the surface of 3DBC-C_3N_4 with ssDNA and ABTS, which accelerated the ABTS affinity for oxidation. Besides negatively charged backbone, ssDNA possesses $\pi-\pi$ interactions and hydrogen bonding via DNA bases. In order to understand the effect in the presence of DNA bases on the TMB substrate binding, varied negatively charged polymers,

DOI: 10.1021/acsami.9b04320
ACS Appl. Mater. Interfaces 2019, 11, 17467−17474

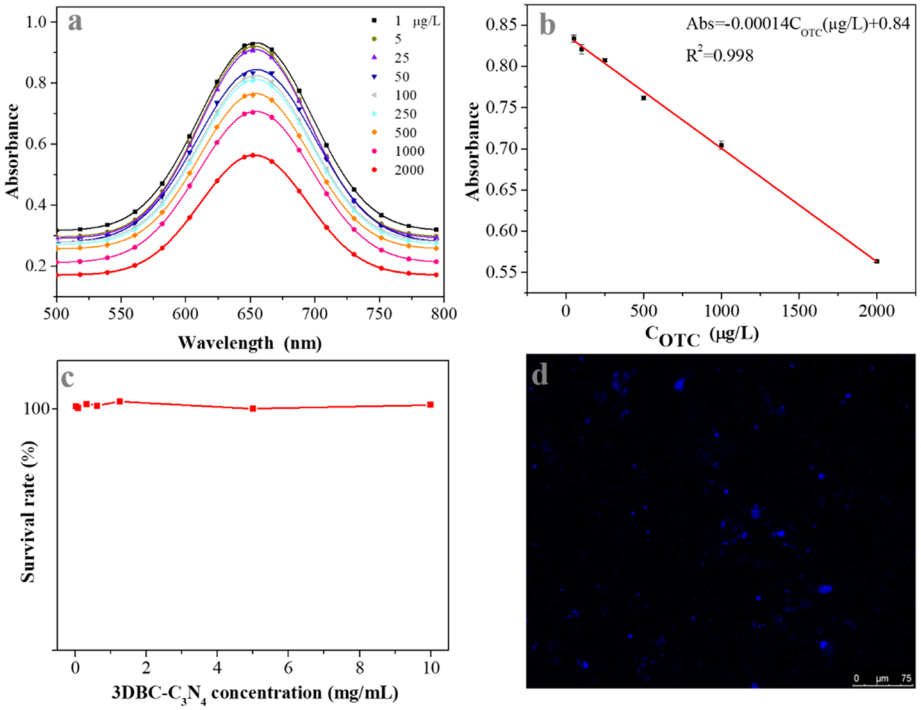

Figure 6. Oxidation of TMB at various OTC concentrations by 3DBC-C_3N_4 with OTC aptamer (a, b). MTT cytotoxicity assay (c) and image of $HepG_2$ cells (d) incubated with 3DBC-C_3N_4.

polystyrene sulfonate (PSS), poly(acrylic acid) (PAA), and deoxy-ribonucleoside triphosphate (dNTP) functionalized 3DBC-C_3N_4 was applied for TMB oxidation. Compared to bare 3DBC-C_3N_4, all modified 3DBC-C_3N_4 exhibited enhanced activity (Figure 5b). PSS, PAA, and dNTP exhibited similar but not obvious enhancement. Even though PAA with a benzene ring structure accelerated the $\pi-\pi$ interaction with 3DBC-C_3N_4, the ssDNA-functionalized 3DBC-C_3N_4 exhibited obvious enhancement. We further proposed that $\pi-\pi$ interaction and hydrogen bonding provided by ssDNA bases also attracted TMB oxidation to some extent. The findings showed that pH affected the peroxidase-like activity of 3DBC-C_3N_4 and also affected the ssDNA and TMB adsorption. To further illustrate the inferences, TMB oxidation on 3DBC-C_3N_4 and 3DBC-C_3N_4 with ssDNA at different pH was tested (Figure 5c). Trend of pH-dependent activity of 3DBC-C_3N_4 with ssDNA remained similar with 3DBC-C_3N_4. The two reactions were found to be more effective at lower pH. Adding ssDNA enhanced the peroxidase-like activity of 3DBC-C_3N_4 at each pH, which further facilitated TMB adsorption. In other words, 3DBC-C_3N_4 with ssDNA can be applied for expanded applications over a broader range.

Application for OTC Detection and Bioimaging. After evaluating the mechanism of ssDNA effect on catalytic activity of 3DBC-C_3N_4, it can be concluded that the effect of OTC aptamer adsorption on enhancing the peroxidase-like activity of 3DBC-C_3N_4 ascribed to both electrostatic attraction and aromatic stacking with TMB substrate. As illustrated in Figure 4b, the amount of TMB oxidation product generated under a fixed reaction condition is positively related to the concentration of OTC aptamer in the system and reaches maximum at 3 μM OTC aptamer, which may be changed by the presence of OTC. We next studied the colorimetric biosensor using 3 μM OTC aptamer as the probe for OTC detection. Colorimetric biosensing was performed for OTC detection using OTC aptamer as the probe. Upon addition of OTC, the adsorption was found to be gradually decreased (Figure 6a). As OTC altered the interaction between aptamer and 3DBC-C_3N_4 in its presence, OTC aptamers were desorbed from 3DBC-C_3N_4 to bind with OTC. The corresponding quantification limit and detection limit were calculated as 50 and 1 μg/L (N = 3), respectively, in the linear detection range from 50 to 2000 μg/L. The regression equation was obtained as Abs = $-0.00014C_{OTC}$ (μg/L) + 0.84 with a correction coefficient (R^2) of 0.998 (Figure 6b), which was comparable to or even better than those of previous strategies (Table S2). The results indicated that a facile colorimetric aptasensor platform based on 3DBC-C_3N_4 nanozyme was successfully established for OTC detection. To elucidate potential risks associated with 3DBC-C_3N_4 for organisms, the cytotoxicity test of $HepG_2$ cells was assessed via standard 3-(4,5-dimethylthiazol-2-yl)-2,5-diphenyltetrazolium bromide (MTT) assay (Figure 6c). As a result, the 3DBC-C_3N_4 was found to be nontoxic and possess good biocompatibility for the organism. Moreover, on the basis of an intensive blue fluorescence of 3DBC-C_3N_4 (Figure S6), it was explored for bioimaging applications in living organisms (Figure 6d) via confocal fluorescence microscopy. The bright blue was clearly observed in $HepG_2$ cells, which suggested 3DBC-C_3N_4 as a promising candidate for intracellular ROS scavenging with bioimaging performance.

CONCLUSIONS

In summary, the 3D branched crystal g-C_3N_4 with one-dimensional nanoneedles was successfully fabricated with a surface area of 73.183 m^2/g and used as nanozymes. The unique sharp edge morphology improved the crystallinity of carbon nitride. The nanoneedles of the prepared 3DBC-C_3N_4 with high curvature on the tip induced accelerated charge collection and separation for H_2O_2 activation. Further, the

DOI: 10.1021/acsami.9b04320
ACS Appl. Mater. Interfaces 2019, 11, 17467−17474

prepared 3DBC-C_3N_4 exhibited excellent peroxidase-like activity in the presence of H_2O_2 and containing TMB substrate. Moreover, the peroxidase-like activity of 3DBC-C_3N_4 was flexibly regulated by ssDNA molecules. The effect mechanism of ssDNA on 3DBC-C_3N_4 was mainly dependent on both electrostatic interaction and aromatic stacking toward chromogenic substrates. Subsequently, a highly sensitive and specific colorimetric aptasensor was successfully constructed for OTC detection. The synergistic effects of 3DBC-C_3N_4 and OTC aptamer enhanced the sensing performance of aptasensor toward OTC. Moreover, 3DBC-C_3N_4 showed high biocompatibility and nontoxicity to $HepG_2$ cells, which suggested its promising implications in intracellular ROS scavenging with bioimaging performance.

■ ASSOCIATED CONTENT

Supporting Information

The Supporting Information is available free of charge on the ACS Publications website at DOI: 10.1021/acsami.9b04320.

Experimental section; graphs of SEM images of 3DBC-C_3N_4 and g-C_3N_4; graphs of pore-size distribution curves and FT-IR of 3DBC-C_3N_4 and g-C_3N_4; graphs of incubated time, pH, concentration of TMB and temperature on peroxidase-like of 3DBC-C_3N_4; table of sequence of nucleic oligomers used in this paper; table of comparison of available sensors for OTC detection (PDF)

■ AUTHOR INFORMATION

Corresponding Author

*E-mail: zhaohuim@dlut.edu.cn.

ORCID

Yanming Liu: 0000-0002-3498-367X

Xie Quan: 0000-0003-3085-0789

Huimin Zhao: 0000-0003-4733-1184

Notes

The authors declare no competing financial interest.

■ ACKNOWLEDGMENTS

This work was supported by the National Natural Science Foundation of China (No. 21777012), the Program of Introducing Talents of Discipline to Universities (B13012), and the Program for Changjiang Scholars and Innovative Research Team in University (IRT_13R05). The authors thank the contributions from Kun Wu and Yi-huan Xu from Fishery College, Huazhong Agricultural University, Wuhan, China.

■ REFERENCES

(1) Wiester, M. J.; Ulmann, P. A.; Mirkin, C. A. Enzyme Mimics Based upon Supramolecular Coordination Chemistry. *Angew. Chem., Int. Ed.* **2011**, *50*, 114−137.

(2) Wei, H.; Wang, E. Nanomaterials with Enzyme-Like Characteristics (Nanozymes): Next-Generation Artificial Enzymes. *Chem. Soc. Rev.* **2013**, *42*, 6060−6093.

(3) Wu, J.; Wang, X.; Wang, Q.; Lou, Z.; Li, S.; Zhu, Y.; Qin, L.; Wei, H. Nanomaterials with Enzyme-Like Characteristics (Nanozymes): Next-Generation Artificial Enzymes (II). *Chem. Soc. Rev.* **2019**, *48*, 1004−1076.

(4) Gao, L.; Zhuang, J.; Nie, L.; Zhang, J.; Zhang, Y.; Gu, N.; Wang, T.; Feng, J.; Yang, D.; Perrett, S.; Yan, X. Intrinsic Peroxidase-Like Activity of Ferromagnetic Nanoparticles. *Nat. Nanotechnol.* **2007**, *2*, 577−583.

(5) Wu, P.; Yan, X. P. Doped Quantum Dots for Chemo/Biosensing and Bioimaging. *Chem. Soc. Rev.* **2013**, *42*, 5489−5521.

(6) Ananthanarayanan, A.; Wang, X.; Routh, P.; Sana, B.; Lim, S.; Kim, D.-H.; Lim, K.-H.; Li, J.; Chen, P. Facile Synthesis of Graphene Quantum Dots from 3D Graphene and their Application for Fe^{3+} Sensing. *Adv. Funct. Mater.* **2014**, *24*, 3021−3026.

(7) Sun, H.; Zhao, A.; Gao, N.; Li, K.; Ren, J.; Qu, X. Deciphering a Nanocarbon-Based Artificial Peroxidase: Chemical Identification of the Catalytically Active and Substrate-Binding Sites on Graphene Quantum Dots. *Angew. Chem., Int. Ed.* **2015**, *54*, 7176−7180.

(8) Wang, J.; Wang, L.; Liu, X.; Liang, Z.; Song, S.; Li, W.; Li, G.; Fan, C. A Gold Nanoparticle-Based Aptamer Target Binding Readout for ATP Assay. *Adv. Mater.* **2007**, *19*, 3943−3946.

(9) Cheng, J.; Di, J.; Hong, J.; Yao, K.; Sun, Y.; Zhuang, J.; Xu, Q.; Zheng, H.; Bi, S. The Promotion Effect of Titania Nanoparticles on the Direct Electrochemistry of Lactate Dehydrogenase Sol-Gel Modified Gold Electrode. *Talanta* **2008**, *76*, 1065−1069.

(10) Liu, B.; Han, X.; Liu, J. Iron Oxide Nanozyme Catalyzed Synthesis of Fluorescent Polydopamine for Light-Up Zn^{2+} Detection. *Nanoscale* **2016**, *8*, 13620−13626.

(11) Song, Y.; Qu, K.; Zhao, C.; Ren, J.; Qu, X. Graphene Oxide: Intrinsic Peroxidase Catalytic Activity and its Application to Glucose Detection. *Adv. Mater.* **2010**, *22*, 2206−2210.

(12) Xia, Y.; Liu, M.; Wang, L.; Yan, A.; He, W.; Chen, M.; Lan, J.; Xu, J.; Guan, L.; Chen, J. A Visible and Colorimetric Aptasensor Based on DNA-Capped Single-Walled Carbon Nanotubes for Detection of Exosomes. *Biosens. Bioelectron.* **2017**, *92*, 8−15.

(13) Lukowski, M. A.; Daniel, A. S.; Meng, F.; Forticaux, A.; Li, L.; Jin, S. Enhanced Hydrogen Evolution Catalysis from Chemically Exfoliated Metallic MoS_2 Nanosheets. *J. Am. Chem. Soc.* **2013**, *135*, 10274−10277.

(14) Ye, L.; Liu, J.; Jiang, Z.; Peng, T.; Zan, L. Facets Coupling of BiOBr-g-C_3N_4 Composite Photocatalyst for Enhanced Visible-Light-Driven Photocatalytic Activity. *Appl. Catal., B* **2013**, *142*−*143*, 1−7.

(15) Li, K.; Zeng, Z.; Yan, L.; Luo, S.; Luo, X.; Huo, M.; Guo, Y. Fabrication of Platinum-Deposited Carbon Nitride Nanotubes by a One-Step Solvothermal Treatment Strategy and their Efficient Visible-Light Photocatalytic Activity. *Appl. Catal., B* **2015**, *165*, 428−437.

(16) Shi, H.; Chen, G.; Zhang, C.; Zou, Z. Polymeric g-C_3N_4 Coupled with $NaNbO_3$ Nanowires toward Enhanced Photocatalytic Reduction of CO_2 into Renewable Fuel. *ACS Catal.* **2014**, *4*, 3637−3643.

(17) Niu, P.; Zhang, L.; Liu, G.; Cheng, H.-M. Graphene-Like Carbon Nitride Nanosheets for Improved Photocatalytic Activities. *Adv. Funct. Mater.* **2012**, *22*, 4763−4770.

(18) Tian, J.; Liu, Q.; Ge, C.; Xing, Z.; Asiri, A. M.; Al-Youbi, A. O.; Sun, X. Ultrathin Graphitic Carbon Nitride Nanosheets: a Low-Cost, Green, and Highly Efficient Electrocatalyst toward the Reduction of Hydrogen Peroxide and its Glucose Biosensing Application. *Nanoscale* **2013**, *5*, 8921−8924.

(19) Yu, H.; Shang, L.; Bian, T.; Shi, R.; Waterhouse, G. I.; Zhao, Y.; Zhou, C.; Wu, L. Z.; Tung, C. H.; Zhang, T. Nitrogen-Doped Porous Carbon Nanosheets Templated from g-C_3N_4 as Metal-Free Electrocatalysts for Efficient Oxygen Reduction Reaction. *Adv. Mater.* **2016**, *28*, 5080−5086.

(20) Tian, J.; Ning, R.; Liu, Q.; Asiri, A. M.; Al-Youbi, A. O.; Sun, X. Three-Dimensional Porous Supramolecular Architecture from Ultrathin g-C_3N_4 Nanosheets and Reduced Graphene Oxide: Solution Self-Assembly Construction and Application as a Highly Efficient Metal-Free Electrocatalyst for Oxygen Reduction Reaction. *ACS Appl. Mater. Interfaces* **2014**, *6*, 1011−1017.

(21) Tian, J.; Liu, Q.; Asiri, A. M.; Alamry, K. A.; Sun, X. Ultrathin Graphitic C_3N_4 Nanosheets/Graphene Composites: Efficient Organic Electrocatalyst for Oxygen Evolution Reaction. *ChemSusChem* **2014**, *7*, 2125−2130.

(22) Wang, Y. Z.; Hao, N.; Feng, Q. M.; Shi, H. W.; Xu, J. J.; Chen, H. Y. A Ratiometric Electrochemiluminescence Detection for Cancer Cells Using g-C_3N_4 Nanosheets and Ag-PAMAM-Luminol Nanocomposites. *Biosens. Bioelectron.* **2016**, *77*, 76−82.
(23) Hu, S.; Ouyang, W.; Guo, L.; Lin, Z.; Jiang, X.; Qiu, B.; Chen, G. Facile Synthesis of Fe_3O_4/g-C_3N_4/HKUST-1 Composites as a Novel Biosensor Platform for Ochratoxin A. *Biosens. Bioelectron.* **2017**, *92*, 718−723.
(24) Xiang, M. H.; Liu, J. W.; Li, N.; Tang, H.; Yu, R. Q.; Jiang, J. H. A Fluorescent Graphitic Carbon Nitride Nanosheet Biosensor for Highly Sensitive, Label-Free Detection of Alkaline Phosphatase. *Nanoscale* **2016**, *8*, 4727−4732.
(25) Tian, J.; Liu, Q.; Asiri, A. M.; Al-Youbi, A. O.; Sun, X. Ultrathin Graphitic Carbon Nitride Nanosheet: a Highly Efficient Fluorosensor for Rapid, Ultrasensitive Detection of Cu^{2+}. *Anal. Chem.* **2013**, *85*, 5595−5599.
(26) Ong, W. J.; Tan, L. L.; Ng, Y. H.; Yong, S. T.; Chai, S. P. Graphitic Carbon Nitride (g-C_3N_4)-Based Photocatalysts for Artificial Photosynthesis and Environmental Remediation: Are We a Step Closer To Achieving Sustainability? *Chem. Rev.* **2016**, *116*, 7159−7329.
(27) Tian, J.; Liu, Q.; Asiri, A. M.; Qusti, A. H.; Al-Youbi, A. O.; Sun, X. Ultrathin Graphitic Carbon Nitride Nanosheets: a Novel Peroxidase Mimetic, Fe Doping-Mediated Catalytic Performance Enhancement and Application to Rapid, Highly Sensitive Optical Detection of Glucose. *Nanoscale* **2013**, *5*, 11604−11609.
(28) Lin, T.; Zhong, L.; Wang, J.; Guo, L.; Wu, H.; Guo, Q.; Fu, F.; Chen, G. Graphite-Like Carbon Nitrides as Peroxidase Mimetics and their Applications to Glucose Detection. *Biosens. Bioelectron.* **2014**, *59*, 89−93.
(29) Qiao, F.; Qi, Q.; Wang, Z.; Xu, K.; Ai, S. MnSe-Loaded g-C_3N_4 Nanocomposite with Synergistic Peroxidase-Like Catalysis: Synthesis and Application toward Colorimetric Biosensing of H_2O_2 and Glucose. *Sens. Actuators, B* **2016**, *229*, 379−386.
(30) Zhang, L.; Li, T.; Li, B.; Li, J.; Wang, E. Carbon Nanotube-DNA Hybrid Fluorescent Sensor for Sensitive and Selective Detection of Mercury(II) Ion. *Chem. Commun.* **2010**, *46*, 1476−1478.
(31) Chehel Amirani, M.; Tang, T. Electrostatics of DNA Nucleotide-Carbon Nanotube Hybrids Evaluated from QM: MM Simulations. *Nanoscale* **2015**, *7*, 19586−19595.
(32) Fan, D.; Zhu, J.; Liu, Y.; Wang, E.; Dong, S. Label-Free and Enzyme-Free Platform for the Construction of Advanced DNA Logic Devices Based on the Assembly of Graphene Oxide and DNA-Templated AgNCs. *Nanoscale* **2016**, *8*, 3834−3840.
(33) Song, J.; Lau, P. S.; Liu, M.; Shuang, S.; Dong, C.; Li, Y. A General Strategy to Create RNA Aptamer Sensors Using "Regulated" Graphene Oxide Adsorption. *ACS Appl. Mater. Interfaces* **2014**, *6*, 21806−21812.
(34) Zhu, Y.; Cai, Y.; Xu, L.; Zheng, L.; Wang, L.; Qi, B.; Xu, C. Building An Aptamer/Graphene Oxide FRET Biosensor for One-Step Detection of Bisphenol A. *ACS Appl. Mater. Interfaces* **2015**, *7*, 7492−7496.
(35) Wang, Q.; Wang, W.; Lei, J.; Xu, N.; Gao, F.; Ju, H. Fluorescence Quenching of Carbon Nitride Nanosheet through Its Interaction with DNA for Versatile Fluorescence Sensing. *Anal. Chem.* **2013**, *85*, 12182−12188.
(36) Park, S.; Shao, Y.; Wan, H.; Rieke, P. C.; Viswanathan, V. V.; Towne, S. A.; Saraf, L. V.; Liu, J.; Lin, Y.; Wang, Y. Design of Graphene Sheets-Supported Pt Catalyst Layer in PEM Fuel Cells. *Electrochem. Commun.* **2011**, *13*, 258−261.
(37) Kobayashi, T.; Kimura, N.; Chi, J.; Hirata, S.; Hobara, D. Channel-Length-Dependent Field-Effect Mobility and Carrier Concentration of Reduced Graphene Oxide Thin-Film Transistors. *Small* **2010**, *6*, 1210−1215.
(38) Huang, J.; Ma, D.; Chen, F.; Bai, M.; Xu, K.; Zhao, Y. Ag Nanoparticles Decorated Cactus-Like Ag Dendrites/Si Nanoneedles as Highly Efficient 3D Surface-Enhanced Raman Scattering Substrates toward Sensitive Sensing. *Anal. Chem.* **2015**, *87*, 10527−10534.
(39) Zhang, N.; Qiao, R.; Su, J.; Yan, J.; Xie, Z.; Qiao, Y.; Wang, X.; Zhong, J. Recent Advances of Electrospun Nanofibrous Membranes in the Development of Chemosensors for Heavy Metal Detection. *Small* **2017**, *13*, No. 1604293.
(40) Saberi Safaei, T.; Mepham, A.; Zheng, X.; Pang, Y.; Dinh, C. T.; Liu, M.; Sinton, D.; Kelley, S. O.; Sargent, E. H. High-Density Nanosharp Microstructures Enable Efficient CO_2 Electroreduction. *Nano Lett.* **2016**, *16*, 7224−7228.
(41) Zeng, Z.; Yu, H.; Quan, X.; Chen, S.; Zhang, S. Structuring Phase Junction between Tri-s-triazine and Triazine Crystalline C_3N_4 for Efficient Photocatalytic Hydrogen Evolution. *Appl. Catal., B* **2018**, *227*, 153−160.
(42) Wang, W.; Wang, D.; Liu, X.; Peng, Q.; Li, Y. Pt-Ni Nanodendrites with High Hydrogenation Activity. *Chem. Commun.* **2013**, *49*, 2903−2905.
(43) Picciolini, S.; Castagnetti, N.; Vanna, R.; Mehn, D.; Bedoni, M.; Gramatica, F.; Villani, M.; Calestani, D.; Pavesi, M.; Lazzarini, L.; Zappettini, A.; Morasso, C. Branched Gold Nanoparticles on ZnO 3D Architecture as Biomedical SERS Sensors. *RSC Adv.* **2015**, *5*, 93644−93651.
(44) Ou, H.; Lin, L.; Zheng, Y.; Yang, P.; Fang, Y.; Wang, X. Tri-s-triazine-Based Crystalline Carbon Nitride Nanosheets for an Improved Hydrogen Evolution. *Adv. Mater.* **2017**, *29*, No. 1700008.
(45) Zhang, G.; Li, G.; Lan, Z. A.; Lin, L.; Savateev, A.; Heil, T.; Zafeiratos, S.; Wang, X.; Antonietti, M. Optimizing Optical Absorption, Exciton Dissociation, and Charge Transfer of a Polymeric Carbon Nitride with Ultrahigh Solar Hydrogen Production Activity. *Angew. Chem., Int. Ed.* **2017**, *56*, 13445−13449.
(46) Zeng, Z.; Quan, X.; Yu, H.; Chen, S.; Zhang, Y.; Zhao, H.; Zhang, S. Carbon Nitride with Electron Storage Property: Enhanced Exciton Dissociation for High-Efficient Photocatalysis. *Appl. Catal., B* **2018**, *236*, 99−106.
(47) Yuan, F.; Zhao, H.; Zang, H.; Ye, F.; Quan, X. Three-Dimensional Graphene Supported Bimetallic Nanocomposites with DNA Regulated-Flexibly Switchable Peroxidase-Like Activity. *ACS Appl. Mater. Interfaces* **2016**, *8*, 9855−9864.
(48) Yang, Z.; Qian, J.; Yang, X.; Jiang, D.; Du, X.; Wang, K.; Mao, H.; Wang, K. A Facile Label-Free Colorimetric Aptasensor for Acetamiprid Based on the Peroxidase-Like Activity of Hemin-Functionalized Reduced Graphene Oxide. *Biosens. Bioelectron.* **2015**, *65*, 39−46.
(49) Niazi, J. H.; Lee, S. J.; Kim, Y. S.; Gu, M. B. ssDNA Aptamers that Selectively Bind Oxytetracycline. *Bioorg. Med. Chem.* **2008**, *16*, 1254−1261.
(50) Liu, B.; Liu, J. Accelerating Peroxidase Mimicking Nanozymes Using DNA. *Nanoscale* **2015**, *7*, 13831−13835.
(51) Hizir, M. S.; Top, M.; Balcioglu, M.; Rana, M.; Robertson, N. M.; Shen, F.; Sheng, J.; Yigit, M. V. Multiplexed Activity of perAuxidase: DNA-Capped AuNPs Act as Adjustable Peroxidase. *Anal. Chem.* **2016**, *88*, 600−605.

DOI: 10.1021/acsami.9b04320
ACS Appl. Mater. Interfaces 2019, 11, 17467−17474